In Situ Fabrication of Lead-Free Double Perovskite/Polymer Composite Films for Optoelectronic Devices and Anticounterfeit Printing

Jindou Shi, Minqiang Wang,* Chen Zhang, Junnan Wang, Yun Zhou, Youlong Xu, Nikolai V. Gaponenko, and Arshad Saleem Bhatti

Read Online

ACCESS | Metrics & More | Article Recommendations | SI Supporting Information

ABSTRACT: Lead-free double perovskites (DP) have the potential to become a rising star in the next generation of lighting markets by addressing the toxicity and instability issues associated with traditional lead-based perovskites. However, high concentrations of hydrochloric acid (HCl) were often employed as a solvent in the preparation of most DPs, accompanied by slow crystallization at high temperatures, which not only raised the risk and cost in the preparation process, but also had a potential threat to the environment. Here, an in situ fabrication strategy was proposed to realize the crystallization of DP in the polymer at low temperature with a mild dimethyl sulfoxide (DMSO) solvent, and subsequently obtained optically well-behaved $Cs_2Na_{0.8}Ag_{0.2}BiCl_6$/PMMA composite films (CFs) by doping with Ag^+, generating

bright orange luminescence with a photoluminescence quantum yield (PLQY) of up to 21.52%. Moreover, the growth dynamics of $Cs_2Na_{0.8}Ag_{0.2}BiCl_6$/PMMA CFs was further investigated by in situ optical transformation, which was extended to other DP-based polymer CFs. Finally, these CFs exhibited excellent performance in optoelectronic devices and anticounterfeit printing, the results of which provide a new pathway to advance the development of lead-free DP materials in the optical field.

KEYWORDS: Lead-free double perovskites, Dimethyl sulfoxide, Composite films, $Cs_2Na_{1-x}Ag_xBiCl_6$/PMMA, Optoelectronic devices
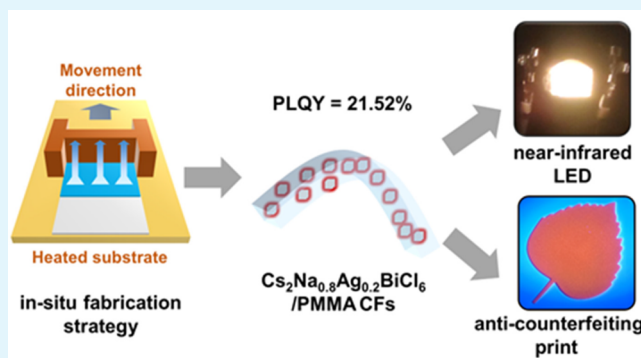
INTRODUCTION

In the past several years, lead halide perovskite $APbX_3$ (A = $CH_3NH_3^+$, Cs^+; X = Cl^-, Br^-, I^-) nanocrystals (NCs) have been considered the most promising material for the next generation of optoelectronic devices benefiting from their excellent optical and electronic properties.[1−5] Unfortunately, the inherent toxicity of Pb^{2+} does not meet current requirements for environmentally friendly materials and seriously limits its application in commercial devices, so the replacement of Pb^{2+} with less toxic or nontoxic elements has become an effective solution and acquired widespread attention.[6−8] Typically, the divalent metal cations employed in the isovalent substitution are very unstable and highly susceptible to oxidation,[9,10] so the combination of monovalent (B^+) and trivalent (B^{3+}) metal cations was adopted to heterovalently substitute Pb^{2+} for synthesis of lead-free double perovskite (DP) as one of the most reliable strategies.[11−14] Currently, the method of obtaining most DPs was by introducing concentrated hydrochloric acid (HCl) as a solvent and growing them at high temperatures for long periods of time.[15] Such a preparation strategy not only adds to the experimental risk and cost but also pollutes the environment

with concentrated HCl,[16] so it is urgent to have a convenient and low-consumption preparation strategy to accomplish the heterovalent substitution of Pb^{2+}.

Nowadays, numerous researchers have synthesized DP materials with a variety of excellent optical properties at different scales utilizing heterovalent substitution, completely overcoming the toxicity of Pb^{2+}.[17−19] The 20% Mn^{2+}-doped $Cs_2Na_{0.2}Ag_{0.8}InCl_6$ DP single crystal (SC) with a maximum emission peak located at 620 nm corresponding to a photoluminescence quantum yield (PLQY) of 32% was acquired by slow crystallization at 180 °C for 50 h through the hydrothermal method in concentrated HCl as a solvent.[20] Besides, $Cs_2AgInCl_6$:Bi NCs with good monodispersity were obtained by rapid injection of cesium oleate solutions into precursors containing HCl at 280 °C employing a fabrication
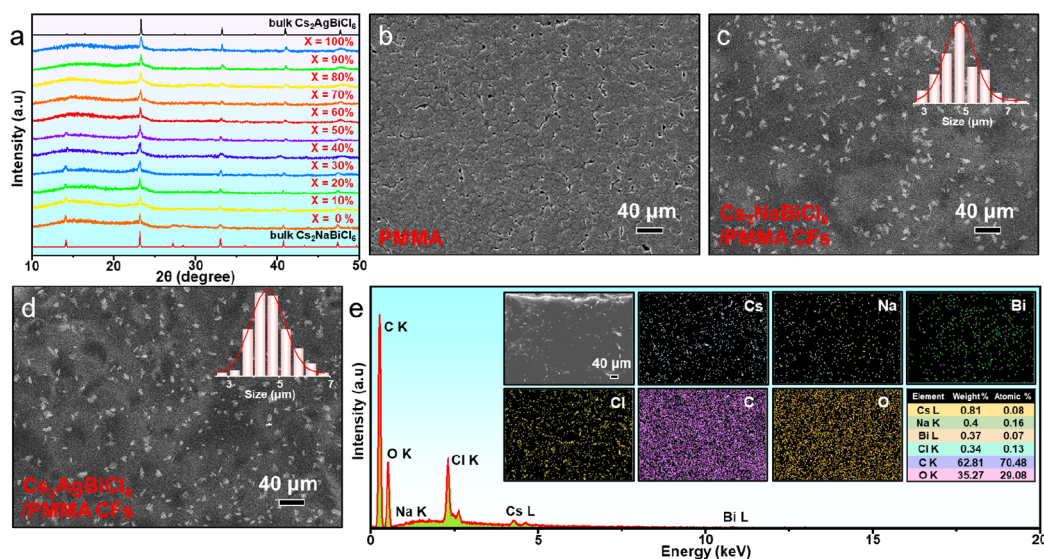
Figure 1. (a) XRD patterns of $Cs_2Na_{1-x}Ag_xBiCl_6$/PMMA CFs with different Ag^+ content (the bottom corresponds to a pure bulk $Cs_2NaBiCl_6$ (ICSD: 2738) and the top to a pure bulk $Cs_2AgBiCl_6$ (ICSD: 291598). SEM images of (b) pure PMMA film, (c) $Cs_2NaBiCl_6$/PMMA CFs and (d) $Cs_2AgBiCl_6$/PMMA CFs. (e) EDS spectrum of $Cs_2NaBiCl_6$/PMMA CFs. The insets in (c) and (d) show the size statistics for $Cs_2NaBiCl_6$ MCs and $Cs_2AgBiCl_6$ MCs in PMMA respectively. The inset in e shows the mapping of elements in the $Cs_2NaBiCl_6$/PMMA CFs as well as the quant results.

method similar to that of lead halide perovskite, where broadband orange emission peaks were observed at 580 nm with PLQY up to 11.4%.[21] It can be seen that although these preparation strategies have resulted in lead-free DPs with excellent optical properties, the inevitable introduction of concentrated HCl and high temperatures in the synthesis process have added to the risk and cost of preparation that does not facilitate further commercial development.

Herein, a strategy for the in situ growth of lead-free DP in polymeric materials to get DP/polymer composite films (CFs) was proposed, which adopted low-risk dimethyl sulfoxide (DMSO) as a precursor solvent to achieve the preparation of high-quality CFs by crystallization at 100 °C for 1 h. Lead-free $Cs_2NaBiCl_6$ was chosen as the DP base and highly transmittance poly methyl methacrylate (PMMA) as the polymer base, resulting in a lower PLQY of the synthesized $Cs_2NaBiCl_6$/PMMA CFs attributed to the indirect band gap structure of $Cs_2NaBiCl_6$.[22] Subsequently, $Cs_2Na_{0.8}Ag_{0.2}BiCl_6$/PMMA CFs with a PLQY of up to 21.52% was further obtained by Ag^+ doping, and monitoring the entire growth process revealed that it mainly consisted of the polymerization of the polymer as well as the crystallization of the DP, which laid the foundation for follow-up exploration. Additionally, this in situ fabrication strategy can be extended to other DP-based polymer CFs, showing some universality. Crucially, these CFs can be industrially prepared on a large scale, which holds great promise in the field of optoelectronic devices and anti-counterfeit printing, promoting the development of lead-free DP materials in the commercial field.

RESULTS AND DISCUSSION

The $Cs_2Na_{1-x}Ag_xBiCl_6$/PMMA CFs with different Ag^+ content was fabricated using a low-cost and low-risk in situ fabrication strategy. In a typical fabrication process, the raw materials of lead-free DP $Cs_2Na_{1-x}Ag_xBiCl_6$ and PMMA were first dissolved in a mild DMSO solvent to form the precursor solution. The choice of DMSO significantly alleviates the risks of preparation and the threat to the environment compared to

conventional processes using concentrated HCl as a solvent. The precursor solution was then uniformly coated onto the substrate using a blade coater. Subsequently, the precursor-coated substrate was gradually heated to 100 °C to promote the formation of DP $Cs_2Na_{1-x}Ag_xBiCl_6$. Finally, the orange-emitting $Cs_2Na_{1-x}Ag_xBiCl_6$/PMMA CFs were formed after holding for 1 h (Specific steps in Experimental Section).

The structure and microscopic morphology of $Cs_2Na_{1-x}Ag_xBiCl_6$/PMMA CFs with different Ag^+ content was further studied by X-ray diffraction (XRD), scanning electron microscope (SEM), and energy-dispersive spectroscopy (EDS) analysis. The XRD patterns of $Cs_2Na_{1-x}Ag_xBiCl_6$/PMMA CFs with different Ag^+ content showed that all samples crystallized in a DP crystal structure and the diffraction peaks were located between bulk $Cs_2NaBiCl_6$ (ICSD: 2738) and bulk $Cs_2AgBiCl_6$ (ICSD: 291598), with no secondary phases observed (Figure 1a). Further observations reveal that the intensity of the (111) plane diffraction peak (2θ angle of 14.14°) of bulk $Cs_2NaBiCl_6$ decreases when the Ag^+ content in the $Cs_2Na_{1-x}Ag_xBiCl_6$/PMMA CFs increases, which is related to the different scattering factor of the Na and Ag atoms.[23] After the doping content of Ag^+ exceeds 60%, the main phase of the $Cs_2Na_{1-x}Ag_xBiCl_6$/PMMA CFs will be presented as a bulk $Cs_2AgBiCl_6$ crystal structure, at which point the (111) plane diffraction peak of bulk $Cs_2NaBiCl_6$ was also no longer observable. Meanwhile, the magnification of XRD in the 22°–25° range indicated that the diffraction peaks were shifted to a higher 2θ angle as the Ag^+ content increased in the $Cs_2Na_{1-x}Ag_xBiCl_6$/PMMA CFs (Figure S1), which can be attributed to the lattice contraction caused by the substitution of Na^+ by smaller Ag^+.[24,25] These results indicate the formation of alloyed DP crystals when working with an intermediate Na/Ag composition. Interestingly, a broader diffraction peak located at 15° was found in the XRD patterns of all CFs, which corresponds exactly to the amorphous PMMA (Figure S2a), implying that the in situ fabrication strategy achieved the growth of $Cs_2Na_{1-x}Ag_xBiCl_6$ inside PMMA. Subsequently, the microscopic morphology of the pure PMMA film obtained by
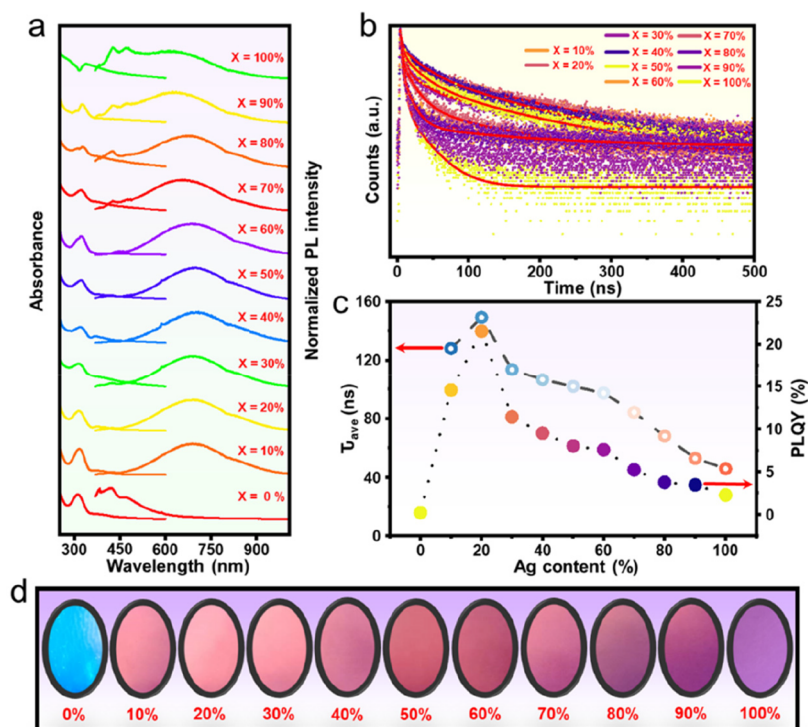
**Figure 2.** (a) Absorbance (left) and normalized PL (right) spectra of $Cs_2Na_{1-x}Ag_xBiCl_6$/PMMA CFs as the Ag^+ content increases (from the bottom curve corresponding to $x = 0\%$, to the top curve corresponding to $x = 100\%$). (b) Time-resolved PL spectra and fitted curves for CFs with different Ag^+ content. (c) The average lifetime τ_{ave} of CFS (hollow circles) and its corresponding PLQYS value (solid circles). (d) Photographs corresponding to $Cs_2Na_{1-x}Ag_xBiCl_6$/PMMA CFs with different Ag^+ content under a 365 nm UV light.

the same fabrication strategy was observed (Figure 1b), and the corresponding SEM image revealing no other crystal material inside and clear colloidal streaks belonging to the conductive adhesive used below, a phenomenon that stems from the high transmittance (97%) of the pure PMMA film (Figure S2d). In contrast, $Cs_2NaBiCl_6$ microcrystals (MCs) and $Cs_2AgBiCl_6$ MCs with an average particle size of approximately 4−5 μm (insets of Figure 1c, d) appear in the $Cs_2NaBiCl_6$/PMMA CFs and $Cs_2AgBiCl_6$/PMMA CFs (Figure 1c, d), respectively, further demonstrating that DP have crystallized within the PMMA, completing the in situ composite of inorganic and organic materials. In addition, information on the chemical structure of $Cs_2NaBiCl_6$ solid-state alloy in PMMA was acquired by Raman spectroscopy. In Figure S3a, the Raman spectra of the pure PMMA film and $Cs_2NaBiCl_6$/PMMA CFs are provided, with both films displaying the strong vibrational peaks of PMMA. Exceptionally, two additional distinct vibrational modes are clearly visible in $Cs_2NaBiCl_6$/PMMA CFs in the 50−500 cm^{-1} range (Figure S3b) and these can be identified as F_{2g} (at 115.7 cm^{-1}) and A_{1g} (at 284.1 cm^{-1}). This pair of strong vibrational modes has been widely reported in pure phase $Cs_2NaBiCl_6$ DP and attributed to the internal vibrations of the $(BiCl_6)^{3-}$ octahedron.[26−28] Subsequently, EDS analysis results for $Cs_2NaBiCl_6$/PMMA CFs (Figure 1e) and $Cs_2AgBiCl_6$/PMMA CFs (Figure S4a-i) further support the in situ formation of DP MCs, with the largest amounts of C and O elements from PMMA and elemental mapping reflecting the homogeneous distribution of $Cs_2NaBiCl_6$ (insets of Figure 1e) and $Cs_2AgBiCl_6$ (Figure S4b-i) in PMMA. At the same time, DP MCs with an average size of 4−5 μm were also found in $Cs_2Na_{1-x}Ag_xBiCl_6$/PMMA CFs with different Ag^+ content

(Figure S5a-i), which confirms that this low-cost and low-risk in situ fabrication strategy can ensure uniform growth of DP MCs in PMMA by adjusting the precursor concentration and film formation temperature. Typically, trace amounts of Ag element were also detected in the EDS analysis result (Figure S6a-i) of the $Cs_2Na_{0.8}Ag_{0.2}BiCl_6$/PMMA CFs with 20% Ag^+ doping, which again reaffirms the successful fabrication of $Cs_2Na_{1-x}Ag_xBiCl_6$/PMMA CFs with different Ag^+ content. The transmittance of the $Cs_2Na_{1-x}Ag_xBiCl_6$/PMMA CFs was also substantially reduced (Figure S7a-k), with only about 50% retained. Afterward, the thicknesses of the pure PMMA film and $Cs_2Na_{0.8}Ag_{0.2}BiCl_6$/PMMA CFs were measured separately, and benefited from being prepared under the same conditions, both remaining at 50 μm (Figure S8), thereby excluding the decay in transmittance caused by the uneven thickness of the polymer. Therefore, the reduced transmittance of $Cs_2Na_{0.8}Ag_{0.2}BiCl_6$/PMMA CFs stemmed mainly from the large number of $Cs_2Na_{0.8}Ag_{0.2}BiCl_6$ particles distributed in the PMMA film, which not only absorbed part of the visible light, but also the large particles prevented the transmission of visible light. These characterization results show that this strategy of using DMSO as a solvent for the in situ fabrication of $Cs_2Na_{1-x}Ag_xBiCl_6$/PMMA CFs can achieve high quality crystallization of $Cs_2Na_{1-x}Ag_xBiCl_6$ in PMMA, with significant saving in cost and reduced experimental risk.

In order to better broaden the prospects of lead-free DP CFs for optoelectronic applications, the optical properties of $Cs_2Na_{1-x}Ag_xBiCl_6$/PMMA CFs have been closely investigated. The UV−vis absorbance spectrum of $Cs_2NaBiCl_6$/PMMA CFs indicated an absorption onset close to 350 nm and a strong exciton absorption peak at 310 nm (Figure 2a), where the pure PMMA film has no absorbance (Figure S2c); therefore it can
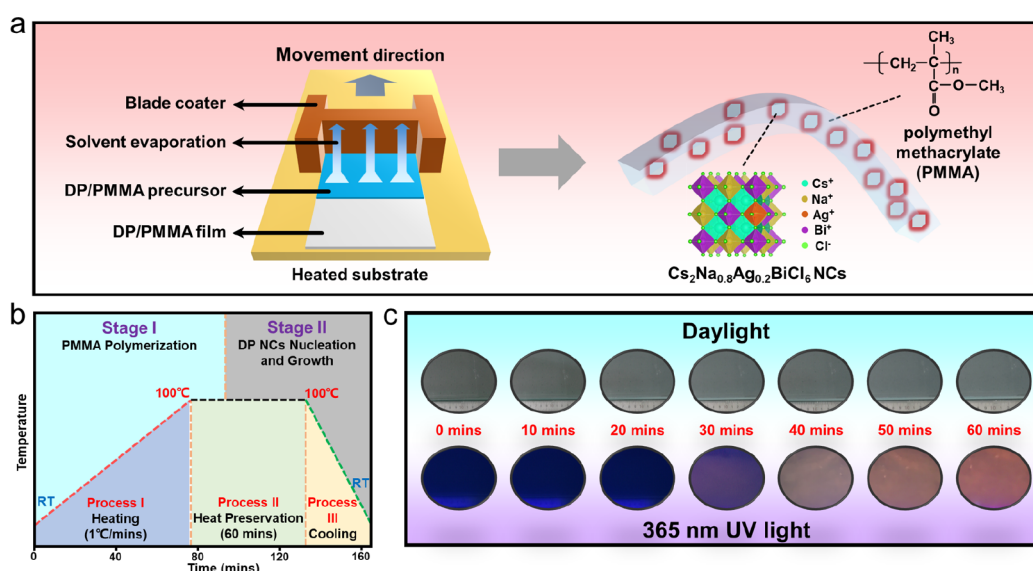
Figure 3. (a) Schematic illustration of the in situ fabrication of $Cs_2Na_{1-x}Ag_xBiCl_6$ embedded PMMA CFs. (b) Analytical diagram of the growth process of $Cs_2Na_{1-x}Ag_xBiCl_6$/PMMA CFs under different classification criteria. (c) Photographs of the corresponding $Cs_2Na_{0.8}Ag_{0.2}BiCl_6$/PMMA CFs under daylight and 365 nm UV light during the heat preservation process (Process II).

be attributed to the $6s^2 \rightarrow 6S\ 2p^1$ transitions of Bi^{3+}.[29] Meanwhile, the PL spectrum exhibits the fluorescence emission peak of $Cs_2NaBiCl_6$/PMMA CFs at 430 nm (Figure 2a), which corresponds exactly to the emission peak of the pure PMMA film (Figure S2b), a phenomenon attributed to the indirect band gap transition of $Cs_2NaBiCl_6$, displaying a remarkably low PLQY that results in the fluorescence being masked by PMMA.[30,31] Therefore, it is essential to modify and extend the electronic and optical properties of $Cs_2NaBiCl_6$/PMMA CFs for its application. According to previous reports, the Cl-p orbital mainly constitutes the valence band maximum (VBM) of $Cs_2NaBiCl_6$, and its conduction band minimum (CBM) comprises mainly Na-s and Bi-p orbitals.[32] However, the energy band composition of $Cs_2AgBiCl_6$ was more complex, with its VBM being composed mainly of Ag-d, Bi-s, and Cl-p orbitals, and its Ag-s, Bi-p, and Cl-p orbitals making up the CBM.[33] Subsequently, doping with different content of Ag^+ allows the Ag-d and Ag-s orbitals to participate in the formation of the VBM and CBM of $Cs_2NaBiCl_6$, thereby contributing to the modification of its electronic structure, which exhibits bright orange-emitting under 365 nm UV light (Figure 2d).[34] As the Ag^+ doping content increased from 0% to 100%, the exciton absorption peak of $Cs_2Na_{1-x}Ag_xBiCl_6$/PMMA CFs was also red-shifted from 310 to 336 nm (Figure 2a and S9a) and a similar phenomenon was observed in its corresponding PL excitation (PLE) spectrum (Figure S10a-j), where the excitation peak was broader in the Ag^+-doped (0% < x < 100%) CFs than in the pure DP ($Cs_2NaBiCl_6$ and $Cs_2AgBiCl_6$) CFs, indicating a gradual transition from $Cs_2NaBiCl_6$/PMMA CFs to $Cs_2AgBiCl_6$/PMMA CFs. However, the position of the main PL emission peak stayed almost the same (at about 690 nm) despite the varying band gap energy of $Cs_2Na_{1-x}Ag_xBiCl_6$/PMMA CFs with Ag^+ doping (Figures 2a and S9a), which in combination with the red-shift phenomenon of the absorption peak caused a gradual decrease of the Stokes shift (Δ_{SS}) from 376 nm at x = 10% to 347 nm at x = 100% (Figure S9b). The above optical properties are mainly attributed to the fact that the emission peak of $Cs_2Na_{1-x}Ag_xBiCl_6$/PMMA CFs originates from the self-

trapped exciton (STE) state PL emission, independent of the energy band edge state. Therefore, the addition of Ag^+ only changed the energy band structure of $Cs_2NaBiCl_6$ without any significant effect on the PL peak position, and its energy band changed as shown in Figure S11. With increasing Ag^+ content, the highest PLQY (21.52%) was achieved at x = 20% for $Cs_2Na_{1-x}Ag_xBiCl_6$/PMMA CFs (Figure 2c), which was attributed to the introduction of extra $[AgCl_6]^{5-}$ octahedrons in $Cs_2NaBiCl_6$ that would separate the original $[NaCl_6]^{5-}$ octahedrons, further modifying the electronic structure of $Cs_2NaBiCl_6$. The introduction of the $[AgCl_6]^{5-}$ octahedrons severely hindered the spatial distribution of the STE state, leading to more holes and electrons being anchored around the adjacent $[NaCl_6]^{5-}$ and $[BiCl_6]^{3-}$ octahedrons, which effectively enhanced the overlap between electron and hole orbitals, making the formation of excitons much easier. On the other hand, the separation of $[NaCl_6]^{5-}$ octahedrons by Ag^+ doping was able to weaken the electron−phonon coupling effect in $Cs_2NaBiCl_6$, thereby effectively enhancing the PLQYs.[35,36] In addition, the interaction between the functional groups such as $-C{=}O$ in PMMA and undercoordinated Ag on the $Cs_2Na_{1-x}Ag_xBiCl_6$ surface can effectively passivate the surface defects by donating extranuclear electrons to the Ag atom,[37,38] which also facilitates the enhancement of PLQYs. As the Ag doping continuously improves, the PLQY drops to 2.27% at x = 100%, at which point the Bi 5c ion in the Ag-rich system are surrounded by $AgCl_6$ octahedra, exhibiting mainly indirect bandgap properties that hinder its STE emission process.[25] Subsequent time-resolved PL measurements showed that the PL decays of all samples were perfectly fitted by a triexponential function (Figure 2b, Table S2), where the short-lived component (τ_1) of the PL decay can be assigned to nonradiative recombination, the middle-lived component (τ_2) assigned to radiative recombination and the long-lived component (τ_3) assigned to emission from the sub-bandgap state.[12] The results of the fitting (Table S2) showed that the radiative recombination rate (A_2) of $Cs_2Na_{1-x}Ag_xBiCl_6$/PMMA CFs first raised and then dropped as the Ag^+ content increased, which was consistent with the trend of its PLQYs,

suggesting that the primary role of Na^+ was to inhibit nonradiative decay pathways competing with the radiative recombination of STE on a similar time scale.[25,39] At x = 20%, the radiative recombination rate of $Cs_2Na_{0.8}Ag_{0.2}BiCl_6$/PMMA CFs reached a maximum of 22.14%, accompanied by its PLQYs at a maximum of 21.52%. In summary, the optical properties of $Cs_2Na_{0.8}Ag_{0.2}BiCl_6$/PMMA CFs obtained by in situ preparation are the most outstanding and offer great opportunities for development.

The crystallization process of $Cs_2Na_{1-x}Ag_xBiCl_6$ in PMMA was further analyzed in order to get a more comprehensive insight into the changes in the optical behaviors of $Cs_2Na_{1-x}Ag_xBiCl_6$/PMMA CFs during the preparation process. It can be seen from the schematic illustration that the in situ fabrication of $Cs_2Na_{1-x}Ag_xBiCl_6$/PMMA CFs using a blade coater was easy (Figure 3a), enabling the crystalline growth of $Cs_2Na_{1-x}Ag_xBiCl_6$ in PMMA by one step, and the whole fabrication process was carried out under open-air environments (25 °C, 30% relative humidity (RH)), greatly reducing production costs, and facilitating large-scale industrial production. The preparation of $Cs_2Na_{1-x}Ag_xBiCl_6$/PMMA CFs consists of three main processes (Figure 3b): Process I (heating), which mainly brings the precursor solution to a suitable temperature (100 °C), thereby ensuring that $Cs_2Na_{1-x}Ag_xBiCl_6$ can crystallized at this temperature; Process II (heat preservation), which focuses on achieving a perfect crystallization process of $Cs_2Na_{1-x}Ag_xBiCl_6$ in PMMA; and Process III (cooling), which collects the prepared $Cs_2Na_{1-x}Ag_xBiCl_6$/PMMA CFs. The crystallization of $Cs_2Na_{1-x}Ag_xBiCl_6$ in PMMA mainly occurred in process II, so $Cs_2Na_{0.8}Ag_{0.2}BiCl_6$/PMMA CFs with the highest PLQY was the selected research subject for a more detailed in situ recording of its optical changes (Figure 3c). It can be seen that during the initial 20 min of heat preservation (100 °C), the CFs do not exhibit fluorescent properties and reflect blue-violet emission under 365 nm UV light, indicating that the $Cs_2Na_{0.8}Ag_{0.2}BiCl_6$ has not yet crystallized at this time, but only PMMA was being polymerized into film. The CFs exhibited weak fluorescence emission at 30 min of heat preservation, and CFs were collected under this condition for further characterization in order to gain insight into the crystallization of $Cs_2Na_{0.8}Ag_{0.2}BiCl_6$ at this time. The results indicate that the lower crystallinity of $Cs_2Na_{0.8}Ag_{0.2}BiCl_6$ in $Cs_2Na_{0.8}Ag_{0.2}BiCl_6$/PMMA CFs obtained by heat preservation for 30 min (Figure S12a) caused the CFs to have a poor PL intensity (Figure S12b) and therefore did not present a significant orange emission under 365 nm UV light (Figure 3c). The excitation (Figure S12b) and absorption (Figure S12c) peaks of the CFs are in the same position as those mentioned previously and the transmittance (Figure S12d) of the CFs was reduced to 50% accompanying the progressive crystallization of $Cs_2Na_{0.8}Ag_{0.2}BiCl_6$ in PMMA. After that, the orange emission of $Cs_2Na_{0.8}Ag_{0.2}BiCl_6$/PMMA CFs also becomes more pronounced with the extended heat preservation time, implying that $Cs_2Na_{0.8}Ag_{0.2}BiCl_6$ has completely crystallized in PMMA by this time. In conclusion, the in situ crystallization of $Cs_2Na_{1-x}Ag_xBiCl_6$ in PMMA can be divided into two stages: Stage I: Before heat preservation for 30 min belongs to the PMMA polymerization stage, where PMMA prefers to polymerize into a film; Stage II: After 30 min of heat preservation belongs to the nucleation and growth stage of $Cs_2Na_{1-x}Ag_xBiCl_6$ inside the PMMA film (Figure 3b). Therefore, the technical key to the in situ preparation of

$Cs_2Na_{0.8}Ag_{0.2}BiCl_6$/PMMA CFs was the controlled polymerization of PMMA and the crystallization of $Cs_2Na_{1-x}Ag_xBiCl_6$. Finally, atomic force microscopy (AFM) 3D images illustrate the surface morphology of the different films prepared using a blade coater in the 5×5 μm^2 area (Figure S13). It can be seen that the surface of the pure PMMA film was uniform, flat and smooth with surface roughness R_q and R_a of 0.342 and 0.272 nm, respectively (Figure S13a), which belong to a remarkably small surface roughness value. Compared to the pure PMMA film, the surface roughness of the in situ fabricated $Cs_2Na_{1-x}Ag_xBiCl_6$ was elevated to around 5 nm (R_q) and 3 nm (R_a) (Figure S13b-d). As a result, the change in the surface morphology of the CFs once again confirms the successful growth of $Cs_2Na_{1-x}Ag_xBiCl_6$ within PMMA, making the surface smoothness fall.

Subsequently, the impact of different heating rates and open-air environments on the in situ fabrication process of $Cs_2Na_{0.8}Ag_{0.2}BiCl_6$/PMMA CFs was explored separately. In order to improve the productivity of CFs, the heating rates in Process I were increased to 5 °C/min and 10 °C/min, respectively. Unfortunately, the too fast heating rate resulted in nonuniform thermal shrinkage of the PMMA polymer, with $Cs_2Na_{0.8}Ag_{0.2}BiCl_6$ enrichment in some regions of CFs (Figure S14a-b), while a slower heating rate (1 °C/min) can overcome this phenomenon allowing $Cs_2Na_{0.8}Ag_{0.2}BiCl_6$ to be grown uniformly in the PMMA. Additionally, the fabrication of $Cs_2Na_{0.8}Ag_{0.2}BiCl_6$/PMMA CFs under high temperature and humidity open-air environments (40 °C, 85% RH; and 40 °C, 90% RH) was simulated, thereby evaluating the universal suitability of the method. The results suggested that the morphology of CFs was not affected by the open-air environments (Figure S15a-b), and their optical properties did not show any weakening, with PLQYs of 21.36% and 20.91% respectively (insets of Figure S15a-b), which are generally consistent with the 21.52% obtained previously. This in situ fabrication strategy can be adapted to extreme open-air environments, attributed to the fact that the precursor solution will be kept at 100 °C for 1 h in Process II, where water will be removed from the DMSO, so that the environmental humidity will have little effect on its preparation. Moreover, the crystallization temperature of CFs was up to 100 °C, so that the room temperature was increased to 40 °C with no significant effect on the preparation process of $Cs_2Na_{0.8}Ag_{0.2}BiCl_6$/PMMA CFs. Especially, the stability of the luminescent material was important for its application in the optical field, so the stability of $Cs_2Na_{0.8}Ag_{0.2}BiCl_6$/PMMA CFs with the most outstanding optical properties was tested under different environments. Benefiting from the protection of the surface hydrophobic PMMA polymer layer, the $Cs_2Na_{0.8}Ag_{0.2}BiCl_6$/PMMA CFs exhibited excellent optical stability in water solution, with its PL intensity remaining essentially unchanged after being immersed in water for 10 h (Figure S16a), and still holding a bright orange emission (inset of Figure S16a). Subsequently, the change in PL intensity of $Cs_2Na_{0.8}Ag_{0.2}BiCl_6$/PMMA CFs as storage time prolonged at different temperatures was explored, and the results showed that the decay trend of its PL intensity became significant with temperature increased (Figure S16b). Furthermore, the instantaneous PL spectra of $Cs_2Na_{0.8}Ag_{0.2}BiCl_6$/PMMA CFs at different temperatures were collected, and it can be seen that the PL intensity decreased with increasing temperature (Figure S17a). The PL intensity of $Cs_2Na_{0.8}Ag_{0.2}BiCl_6$/PMMA CFs was increased when the temperature returned to room
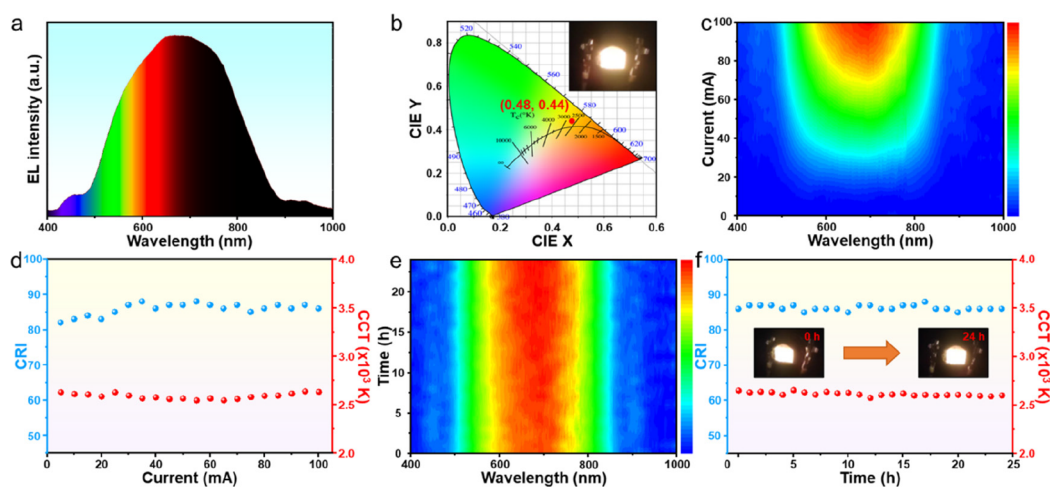
Figure 4. (a) EL spectrum and (b) CIE color coordinate of the NIR LED assembled for $Cs_2Na_{0.8}Ag_{0.2}BiCl_6$/PMMA CFs. Changes in the (c) EL spectra, (d) CRI (blue point), and CCT (red point) of NIR LED at different drive currents. Changes in the (e) EL spectra, (f) CRI (blue point) and CCT (red point) of NIR LED driven by 100 mA current with extended operating time (24 h). The inset in (b) is photographs of the corresponding NIR LED in operation. The insets in (f) are photographs of the corresponding NIR LED before and after 24 h of operation, respectively.

temperature; however it was unable to recover to the initial PL intensity (Figure S17b). A similar phenomenon has been reported in lead halide perovskite,[40] which derived from the appearance of different trap states within $Cs_2Na_{0.8}Ag_{0.2}BiCl_6$ after heating, where recoverable PL belonging to temporary defect states and irrecoverable PL from permanent defect states. At the same time, the PL intensity loss ratio of $Cs_2Na_{0.8}Ag_{0.2}BiCl_6$/PMMA CFs was calculated to be 31% (Figure S17c), which was lower than that of the lead halide perovskite/polymer CFs,[41] indicating that the lead-free perovskite structure was more stable than the lead halide perovskite. Correspondingly, the PL peak position of $Cs_2Na_{0.8}Ag_{0.2}BiCl_6$/PMMA CFs showed a blue shift when the temperature increased to 363 K (Figure S17d), which was due to the out-of-phase band-edge states stabilized as lattice dilation at the Brillouin zone boundary.[42] The above stability tests indicated that the excellent water stability of $Cs_2Na_{0.8}Ag_{0.2}BiCl_6$/PMMA CFs allowed it to be suitable for optoelectronic devices under high humidity environments, setting the stage for its subsequent commercial development.

Remarkably, this strategy for the in situ fabrication of DP/polymer CFs was versatile and can be extended to other DP-based polymer CFs. Through screening of the polymers, polyvinylidene difluoride (PVDF) was selected as the polymer phase benefiting from its ability to be well soluble in DMSO. $Cs_2Na_{0.8}Ag_{0.2}BiCl_6$/PVDF CFs was obtained employing the same preparation method as before, with SEM image showing that $Cs_2Na_{0.8}Ag_{0.2}BiCl_6$ with an average particle size of approximately 5 μm were also observed in PVDF (Figure S18a), which are consistent with the previous results in $Cs_2Na_{0.8}Ag_{0.2}BiCl_6$/PMMA CFs, further suggesting that the crystallization of $Cs_2Na_{1-x}Ag_xBiCl_6$ was independent of the choice of polymer. EDS analysis demonstrated that besides the constituent elements of $Cs_2Na_{0.8}Ag_{0.2}BiCl_6$, strong signals of elements C and F were detected, which derived from PVDF (Figure S18b-j). Subsequently, further characterization results revealed that the crystallinity of $Cs_2Na_{0.8}Ag_{0.2}BiCl_6$ in the $Cs_2Na_{0.8}Ag_{0.2}BiCl_6$/PVDF CFs in situ fabricated at 100 °C remained high (Figure S19a), and that it also emitted bright orange light at 690 nm (Figure S19b), corresponding to a

PLQY value of 18.41%. Furthermore, the PLE (Figure S19b), absorbance (Figure S19c) and transmittance (Figure S19d) spectra of $Cs_2Na_{0.8}Ag_{0.2}BiCl_6$/PVDF CFs obtained by the same method are in general agreement with those of $Cs_2Na_{0.8}Ag_{0.2}BiCl_6$/PMMA CFs reported previously. The distinction was that the surface roughness R_q and R_a of the pure PVDF film reached 5.19 and 3.08 nm respectively (Figure S20a), which was not sufficiently smooth compared to the pure PMMA film. Eventually, the surface roughness of $Cs_2Na_{0.8}Ag_{0.2}BiCl_6$/PVDF CFs increases again to 9.38 nm (R_q) and 6.97 nm (R_a) when $Cs_2Na_{0.8}Ag_{0.2}BiCl_6$ has finished crystallizing in PVDF (Figure S20b). The above characterization results reinforce the universality of this in situ fabrication strategy for DP/polymer CFs and provide a solid basis for the future development of DPs. To facilitate overall comparison, Table S2 lists some other fabrication strategies for lead-free DP and their main optical parameters. Compared to other preparation strategies, the in situ fabrication of DP/polymer CFs does not require the use of concentrated HCl, which greatly alleviates the risk of experimental and environmental pollution, and the reaction temperature and time are simultaneously lowered, allowing for effective cost savings in production. Moreover, the introduction of the blade coater has simplified the fabrication process and made it more suitable for large-scale production, which will enable DP/polymer CFs to play an indispensable role in the future of the optical field.

The PL spectra of $Cs_2Na_{1-x}Ag_xBiCl_6$/PMMA CFs indicate an ultrawide emission covering the near-infrared (NIR) region, which renders them potentially promising for applications in NIR spectral detection and night vision. Subsequently, the $Cs_2Na_{0.8}Ag_{0.2}BiCl_6$/PMMA CFs with the highest PLQY value was selected to be assembled with a commercial 365 nm UV LED chip to form a NIR LED and to further investigate its optoelectronic properties. As can be seen from the electroluminescence (EL) spectrum of the NIR LED (Figure 4a), its emission range extends from the visible region to the NIR region, in general agreement with the PL spectrum obtained as before, with the position of the emission peak center shifted to 680 nm, which stems from the inconsistent angle of the excitation source. The international commission on illumina-
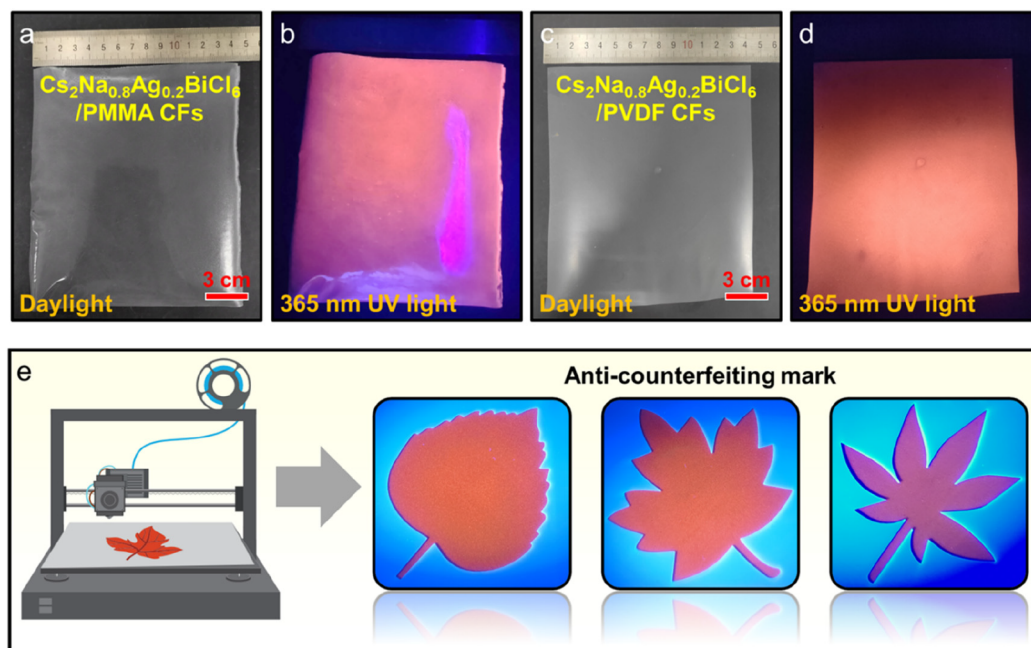
Figure 5. Optical images of the large size (a, b) $Cs_2Na_{0.8}Ag_{0.2}BiCl_6$/PMMA CFs and (c, d) $Cs_2Na_{0.8}Ag_{0.2}BiCl_6$/PVDF CFs prepared in situ under daylight and 365 nm UV light, respectively. (e) Diagram of the anticounterfeiting print and the printed anticounterfeiting mark consisting of $Cs_2Na_{0.8}Ag_{0.2}BiCl_6$/PMMA CFs.

tion (CIE) diagram for NIR LED displays the corresponding color coordinate as (0.48, 0.44) (Figure 4b), and the color area in which this coordinate positioned is consistent with the color of the device emission as observed by the naked eye, both appearing distinctly orange (inset of Figure 4b). The EL spectra of the NIR LED at different drive currents were recorded, no significant differences can be seen in the shape of the spectra and the position of the emission peaks, suggesting good current drive stability of the device (Figure 4c). In addition, no apparent saturation of the EL intensity was observed with increasing current, which indicates that the NIR LED assembled from $Cs_2Na_{0.8}Ag_{0.2}BiCl_6$/PMMA CFs are suitable for high-power lighting systems. At the same time, the color-rendering index (CRI) of NIR LED remains essentially at a relatively high value of 85 when the injection current ranges from 5 to 100 mA, and its correlated color temperature (CCT) display remains at approximately 2600 K, indicating a high emission purity at different drive currents (Figure 4d). Finally, the most significant evaluation criterion for the performance of optoelectronic devices was their long-term operating stability, so the changes in the EL spectra and intensity of NIR LED were monitored over a 24 h period at a high current of 100 mA. The results reveal that the EL spectra of NIR LED are almost unchanged and its main emission peak intensity at 680 nm matches the initial intensity, which is contributed to the extremely high optical stability of $Cs_2Na_{0.8}Ag_{0.2}BiCl_6$/PMMA CFs, unaffected by the UV chip (Figure 4e). Furthermore, the CRI of the device was also settled at 85 for different operating times, and its CCT display remained at 2600 K after 24 h of operation (Figure 4f). The combination of the above practical optoelectronic applications suggests that $Cs_2Na_{1-x}Ag_xBiCl_6$/PMMA CFs have high optical stability and that the excellent operating performance exhibited by its assembly into NIR LED will provide a new option for the development of night vision tools.

Whether optical materials can be fabricated on a large scale will directly determine their future business promotion and application. Here, the preparation of large-size DP/polymer CFs was explored in depth to ensure that the strategy of in situ grown $Cs_2Na_{1-x}Ag_xBiCl_6$/PMMA CFs and $Cs_2Na_{1-x}Ag_xBiCl_6$/PVDF CFs has a high practical application value. Through scaling up the dosage of precursors in the same proportions, large sizes (14×18 cm^2) of $Cs_2Na_{0.8}Ag_{0.2}BiCl_6$/PMMA CFs and $Cs_2Na_{0.8}Ag_{0.2}BiCl_6$/PVDF CFs were obtained, with other preparation conditions being unchanged (Figure 5a, c). As can be seen in the optical image under the 365 nm UV light, $Cs_2Na_{0.8}Ag_{0.2}BiCl_6$ was distributed very uniformly in PMMA and PVDF with a bright orange fluorescent emitted from both large-scale CFs (Figure 5b, d). On the other hand, $Cs_2Na_{0.8}Ag_{0.2}BiCl_6$/PMMA CFs can be further applied to optical anticounterfeiting prints with the advantage that it is colorless and translucent in daylight (Figure 5a, c). The precursor solution of $Cs_2Na_{0.8}Ag_{0.2}BiCl_6$/PMMA CFs was processed into different patterns using inkjet printing technology, and then heated to complete the polymerization and crystallization for a high-quality anticounterfeiting mark, which displays an orange anticounterfeiting pattern under 365 nm UV light (Figure 5e). This versatile development of $Cs_2Na_{0.8}Ag_{0.2}BiCl_6$/PMMA CFs and $Cs_2Na_{0.8}Ag_{0.2}BiCl_6$/PVDF CFs will greatly improve their impact in the next generation of optical materials, furthermore allowing large scale in situ fabrication of DP/polymer CFs will also accelerate its commercialization.

■ CONCLUSION

In summary, we have proposed a convenient and low-consumption synthetic strategy for the in situ fabrication of $Cs_2Na_{1-x}Ag_xBiCl_6$/PMMA CFs using DMSO as a solvent at a lower temperature (100 °C), and analyzed in detail the complete crystallization process of $Cs_2Na_{1-x}Ag_xBiCl_6$ in PMMA. Compared to the traditional method of using

concentrated hydrochloric acid as a solvent and slow crystallization at high temperatures, this method considerably lowers the cost and risk of preparation, preventing environmental pollution. Especially, the $Cs_2Na_{0.8}Ag_{0.2}BiCl_6$/PMMA CFs with 20% Ag^+ doping exhibited enhanced PL performance under 365 nm UV light with an ultrawide emission wavelength covering the NIR region, corresponding to a PLQY of 21.52%. On this basis, the $Cs_2Na_{0.8}Ag_{0.2}BiCl_6$/PVDF CFs with the same emission wavelength was obtained by changing the composition of the polymer precursors, indicating the universality of this fabrication strategy. Moreover, the CFs were capable of large-scale industrial production, which paved the way for a subsequent commercialization process. More importantly, the CFs have an outstanding performance in the field of night vision as well as optical anticounterfeiting, so we believe this in situ synthesis strategy will dramatically facilitate the development of the lead-free DP, opening the door for future applications of DP/polymer CFs in flexible optics.

■ EXPERIMENTAL SECTION

Materials. The cesium chloride (CsCl, 99.99%), sodium chloride (NaCl, 99.5%), silver chloride (AgCl, 99.5%), bismuth chloride (BiCl₃, 99.99%), and dimethyl sulfoxide (DMSO, 99%) were purchased from Aladdin. The poly methyl methacrylate (PMMA) and poly(vinylidene fluoride) (PVDF) purchased from Macklin and Alfa Aesar, respectively. All the reagents were used without further purification.

Fabrication of $Cs_2Na_{1-x}Ag_xBiCl_6$/PMMA CFs with Different Ag^+ Content. The in situ fabrication of $Cs_2Na_{1-x}Ag_xBiCl_6$/PMMA CFs consists of two main stages. Stage I: Preparation of the precursor solution and coating of the film. The precursor solution included 0.06 mmol CsCl, 0.03-X mmol NaCl (X = 0, 0.003, 0.006, 0.009, 0.012, 0.015, 0.018, 0.021, 0.024, 0.027, 0.03), X mmol AgCl and 0.03 mmol BiCl₃ in 10 mL of DMSO solvent with continuous stirring until complete dissolution. Subsequently, 1 g of PMMA particles was added to the mixed solution and stirred at 60 °C for 30 min until the PMMA particles were dissolved and finally cooled to room temperature. The above precursor solution was then applied uniformly to the substrate using a blade applicator to form a film. Stage II: The precursor coated substrate was gradually heated (1 °C/min) to 100 °C to promote the formation of DP $Cs_2Na_{1-x}Ag_xBiCl_6$. Afterward, the film was held at 100 °C for 1 h until the $Cs_2Na_{1-x}Ag_xBiCl_6$ was completely crystallized. Finally, $Cs_2Na_{1-x}Ag_xBiCl_6$/PMMA CFs was obtained by natural cooling to room temperature.

Fabrication of $Cs_2Na_{1-x}Ag_xBiCl_6$/PVDF CFs with Different Ag^+ Content. All steps are the same as for the fabrication of $Cs_2Na_{1-x}Ag_xBiCl_6$/PMMA CFs, except that 1 g of PMMA particles are replaced by 1 g of PVDF powder, which can be dissolved at room temperature.

NIR LED Device Assembled by $Cs_2Na_{0.8}Ag_{0.2}BiCl_6$/PMMA CFs. To achieve a near-infrared emitting LED, $Cs_2Na_{0.8}Ag_{0.2}BiCl_6$/PMMA CFs was cut to the right size and placed on the surface of a commercial UV LED chip (365 nm, EP-U4545K-A3, 3.7 V, 5W, Guanghong Technology, China) to be assembled into NIR LED device.

Characterization Methods. The morphology and EDS spectra of films were investigated by field emission scanning electron microscopy (SEM, FEI Quatan FEG 250) equipped with an energy dispersive spectrometer (EDS). The surface roughness of the films is obtained from atomic force microscopy (AFM, INNOVA). The photoluminescence (PL) spectra, PL quantum yields (PLQYs) and time-resolved PL (TRPL) decay curves were recorded on an Edinburgh Instruments FLS 1000 spectrometer. The ultraviolet—visible (UV—vis) absorption and transmittance spectra were recorded by PE Lambda 950. The X-ray diffraction (XRD) patterns were obtained using the DB-ADVANCE X-ray diffraction analyzer diffractometer. The PL spectra of the samples at different temperatures were collected by Photo Research 670 spectrometer after heating the samples using a heater (MS7—H550-S, DLAB, China) and under 365 nm UV light irradiation. The EL spectra of NIR LED were collected by a Keithley 2400 sourcemeter and a Photo Research 670 spectrometer. Raman experiments were performed on a HR Evolution-800 Raman microscope system (Horiba), equipped with standard 532 nm laser sources. High temperature and high humidity chambers (BDX-30F DONGGUAN BEIDOUXING TESTING EQUIPMENT CO. LTD) were adopted to provide constant humidity for the preparation of composite films in high humidity environments.

■ ASSOCIATED CONTENT

Ⓢ Supporting Information

The Supporting Information is available free of charge at https://pubs.acs.org/doi/10.1021/acsami.2c22752.

XRD, SEM, and EDS data of CFs, Raman spectra, Transmittance spectra, PLE spectra, AFM topographies images of CFs, Energy band structure, water and thermal stability testing of CFs (Figures S1—S20), fitting results of PL decays, and comparison of our work and previous references (Tables S1 and S2) (PDF)

■ AUTHOR INFORMATION

Corresponding Author

Minqiang Wang — *Electronic Materials Research Laboratory, Key Laboratory of the Ministry of Education International Center for Dielectric Research & Shannxi Engineering Research Center of Advanced Energy Materials and Devices, Xi'an Jiaotong University, 710049 Xi'an, China;* Email: mqwang@xjtu.edu.cn

Authors

Jindou Shi — *Electronic Materials Research Laboratory, Key Laboratory of the Ministry of Education International Center for Dielectric Research & Shannxi Engineering Research Center of Advanced Energy Materials and Devices, Xi'an Jiaotong University, 710049 Xi'an, China;* ⓞ orcid.org/0000-0003-1082-5009

Chen Zhang — *Electronic Materials Research Laboratory, Key Laboratory of the Ministry of Education International Center for Dielectric Research & Shannxi Engineering Research Center of Advanced Energy Materials and Devices, Xi'an Jiaotong University, 710049 Xi'an, China*

Junnan Wang — *Electronic Materials Research Laboratory, Key Laboratory of the Ministry of Education International Center for Dielectric Research & Shannxi Engineering Research Center of Advanced Energy Materials and Devices, Xi'an Jiaotong University, 710049 Xi'an, China;* ⓞ orcid.org/0000-0002-3074-0195

Yun Zhou — *Electronic Materials Research Laboratory, Key Laboratory of the Ministry of Education International Center for Dielectric Research & Shannxi Engineering Research Center of Advanced Energy Materials and Devices, Xi'an Jiaotong University, 710049 Xi'an, China*

Youlong Xu — *Electronic Materials Research Laboratory, Key Laboratory of the Ministry of Education International Center for Dielectric Research & Shannxi Engineering Research Center of Advanced Energy Materials and Devices, Xi'an Jiaotong University, 710049 Xi'an, China*

Nikolai V. Gaponenko — *Belarusian State University of Informatics and Radioelectronics, 220013 Minsk, Belarus*

Arshad Saleem Bhatti − *Centre for Micro and Nano Devices, Department of Physics, COMSATS Institute of Information Technology, Islamabad 44500, Pakistan*

Complete contact information is available at:
https://pubs.acs.org/10.1021/acsami.2c22752

Notes
The authors declare no competing financial interest.

■ REFERENCES

(1) Song, J. Z.; Li, J. H.; Li, X. M.; Xu, L. M.; Dong, Y. H.; Zeng, H. B. Quantum Dot Light-Emitting Diodes Based on Inorganic Perovskite Cesium Lead Halides (CsPbX$_3$). *Adv. Mater.* **2015**, *27*, 7162−7167.

(2) Wei, C. T.; Su, W. M.; Li, J. T.; Xu, B.; Shan, Q. S.; Wu, Y.; Zhang, F. J.; Luo, M. M.; Xiang, H. Y.; Cui, Z.; Zeng, H. B. A Universal Ternary-Solvent-Ink Strategy toward Efficient Inkjet-Printed Perovskite Quantum Dot Light-Emitting Diodes. *Adv. Mater.* **2022**, *34*, 2107798.

(3) Huang, X. J.; Guo, Q. Y.; Yang, D. D.; Xiao, X. D.; Liu, X. F.; Xia, Z. G.; Fan, F. J.; Qiu, J. R.; Dong, G. P. Reversible 3D Laser Printing of Perovskite Quantum Dots inside A Transparent Medium. *Nat. Photonics* **2020**, *14*, 82−88.

(4) Bohn, B. J.; Tong, Y.; Gramlich, M.; Lai, M. L.; Doblinger, M.; Wang, K.; Hoye, R. L. Z.; Muller-Buschbaum, P.; Stranks, S. D.; Urban, A. S.; Polavarapu, L.; Feldmann, J. Boosting Tunable Blue Luminescence of Halide Perovskite Nanoplatelets through Post-synthetic Surface Trap Repair. *Nano Lett.* **2018**, *18*, 5231−5238.

(5) Shamsi, J.; Urban, A. S.; Imran, M.; De Trizio, L.; Manna, L. Metal Halide Perovskite Nanocrystals: Synthesis, Post-Synthesis Modifications, and Their Optical Properties. *Chem. Rev.* **2019**, *119*, 3296−3348.

(6) Fu, H. Y. Review of Lead-Free Halide Perovskites as Light-Absorbers for Photovoltaic Applications: From Materials to Solar Cells. *Sol Energ Mat Sol C* **2019**, *193*, 107−132.

(7) Ghosh, S.; Pradhan, B. Lead-Free Metal Halide Perovskite Nanocrystals: Challenges, Applications, and Future Aspects. *Chemnanomat* **2019**, *5*, 300−312.

(8) Fan, Q. Q.; Biesold-McGee, G. V.; Ma, J. Z.; Xu, Q. N.; Pan, S.; Peng, J.; Lin, Z. Q. Lead-Free Halide Perovskite Nanocrystals: Crystal Structures, Synthesis, Stabilities, and Optical Properties. *Angew. Chem. Int. Edit* **2020**, *59*, 1030−1046.

(9) Jellicoe, T. C.; Richter, J. M.; Glass, H. F. J.; Tabachnyk, M.; Brady, R.; Dutton, S. E.; Rao, A.; Friend, R. H.; Credgington, D.; Greenham, N. C.; Bohm, M. L. Synthesis and Optical Properties of Lead-Free Cesium Tin Halide Perovskite Nanocrystals. *J. Am. Chem. Soc.* **2016**, *138*, 2941−2944.

(10) Wu, X. T.; Song, W. D.; Li, Q.; Zhao, X. X.; He, D. S.; Quan, Z. W. Synthesis of Lead-Free CsGeI$_3$ Perovskite Colloidal Nanocrystals and Electron Beam-induced Transformations. *Chem-Asian J.* **2018**, *13*, 1654−1659.

(11) Bekenstein, Y.; Dahl, J. C.; Huang, J. M.; Osowiecki, W. T.; Swabeck, J. K.; Chan, E. M.; Yang, P. D.; Alivisatos, A. P. The Making and Breaking of Lead-Free Double Perovskite Nanocrystals of Cesium Silver-Bismuth Halide Compositions. *Nano Lett.* **2018**, *18*, 3502−3508.

(12) Yang, B.; Chen, J. S.; Yang, S. Q.; Hong, F.; Sun, L.; Han, P. G.; Pullerits, T.; Deng, W. Q.; Han, K. L. Lead-Free Silver-Bismuth Halide Double Perovskite Nanocrystals. *Angew. Chem. Int. Edit* **2018**, *57*, 5359−5363.

(13) Yang, B.; Hong, F.; Chen, J. S.; Tang, Y. X.; Yang, L.; Sang, Y. B.; Xia, X. S.; Guo, J. W.; He, H. X.; Yang, S. Q.; Deng, W. Q.; Han, K. L. Colloidal Synthesis and Charge-Carrier Dynamics of Cs$_2$AgSb$_{1-y}$Bi$_y$X$_6$ (X: Br, Cl; $0 \leq y \leq 1$) Double Perovskite Nanocrystals. *Angew. Chem. Int. Edit* **2019**, *58*, 2278−2283.

(14) Igbari, F.; Wang, Z. K.; Liao, L. S. Progress of Lead-Free Halide Double Perovskites. *Adv. Energy Mater.* **2019**, *9*, 1803150.

(15) Liu, Y.; Nag, A.; Manna, L.; Xia, Z. G. Lead-Free Double Perovskite Cs$_2$AgInCl$_6$. *Angew. Chem. Int. Edit* **2021**, *60*, 11592−11603.

(16) Evans, C. D.; Monteith, D. T.; Fowler, D.; Cape, J. N.; Brayshaw, S. Hydrochloric Acid: An Overlooked Driver of Environmental Change. *Environ. Sci. Technol.* **2011**, *45*, 1887−1894.

(17) Li, S.; Shi, Z. F.; Zhang, F.; Wang, L. T.; Ma, Z. Z.; Wu, D.; Yang, D. W.; Chen, X.; Tian, Y. T.; Zhang, Y. T.; Shan, C. X.; Li, X. J. Ultrastable Lead-Free Double Perovskite Warm-White Light-Emitting Devices with A Lifetime above 1000 h. *ACS Appl. Mater. Inter* **2020**, *12*, 46330−46339.

(18) Yin, H.; Xian, Y. M.; Zhang, Y. L.; Chen, W. J.; Wen, X. M.; Rahman, N. U.; Long, Y.; Jia, B. H.; Fan, J. D.; Li, W. Z. An Emerging Lead-Free Double-Perovskite Cs$_2$AgFeCl$_6$:In Single Crystal. *Adv. Funct Mater.* **2020**, *30*, 2002225.

(19) Ahmad, R.; Zdrazil, L.; Kalytchuk, S.; Naldoni, A.; Rogach, A. L.; Schmuki, P.; Zboril, R.; Kment, S. Uncovering the Role of Trioctylphosphine on Colloidal and Emission Stability of Sb-Alloyed Cs$_2$NaInCl$_6$ Double Perovskite Nanocrystals. *ACS Appl. Mater. Inter* **2021**, *13*, 47845−47859.

(20) Zheng, W.; Li, X. L.; Liu, N. Q.; Yan, S.; Wang, X. J.; Zhang, X. Z.; Liu, Y. Q.; Liang, Y. J.; Zhang, Y. H.; Liu, H. Solution-Grown Chloride Perovskite Crystal of Red Afterglow. *Angew. Chem. Int. Edit* **2021**, *60*, 24450−24455.

(21) Liu, Y.; Jing, Y. Y.; Zhao, J.; Liu, Q. L.; Xia, Z. G. Design Optimization of Lead-Free Perovskite Cs$_2$AgInCl$_6$:Bi Nanocrystals with 11.4% Photoluminescence Quantum Yield. *Chem. Mater.* **2019**, *31*, 3333−3339.

(22) Morss, L. R.; Siegal, M.; Stenger, L.; Edelstein, N. Preparation of Cubic Chloro Complex Compounds of Trivalent Metals - Cs$_2$NaMCl$_6$. *Inorg. Chem.* **1970**, *9*, 1771−1775.

(23) Lim, T. W.; Kim, S. D.; Sung, K. D.; Rhyim, Y. M.; Jeen, H.; Yun, J.; Kim, K. H.; Song, K. M.; Lee, S.; Chung, S. Y.; Choi, M.; Choi, S. Y. Insights into Cationic Ordering in Re-Based Double Perovskite Oxides. *Sci. Rep* **2016**, *6*, 19746.

(24) Luo, J. J.; Wang, X. M.; Li, S. R.; Liu, J.; Guo, Y. M.; Niu, G. D.; Yao, L.; Fu, Y. H.; Gao, L.; Dong, Q. S.; Zhao, C. Y.; Leng, M. Y.; Ma, F. S.; Liang, W. X.; Wang, L. D.; Jin, S. Y.; Han, J. B.; Zhang, L. J.; Etheridge, J.; Wang, J. B.; Yan, Y. F.; Sargent, E. H.; Tang, J. Efficient and Stable Emission of Warm-White Light from Lead-Free Halide Double Perovskites. *Nature* **2018**, *563*, 541−545.

(25) Zhu, D. X.; Zito, J.; Pinchetti, V.; Dang, Z. Y.; Olivati, A.; Pasquale, L.; Tang, A. W.; Zaffalon, M. L.; Meinardi, F.; Infante, I.; De Trizio, L.; Manna, L.; Brovelli, S. Compositional Tuning of Carrier Dynamics in Cs$_2$Na$_{1-x}$Ag$_x$BiCl$_6$ Double-Perovskite Nanocrystals. *ACS Energy Lett.* **2020**, *5*, 1840−1847.

(26) Pelle, F.; Blanzat, B.; Chevalier, B. Low-Temperature Phase-Transition in Cubic Elpasolithe Crystal Cs$_2$NaBiCl$_6$. *Solid State Commun.* **1984**, *49*, 1089−1093.

(27) Smit, W. M. A.; Dirksen, G. J.; Stufkens, D. J. Infrared and Raman-Spectra of the Elpasolites Cs$_2$NaSbCl$_6$ and Cs$_2$NaBiCl$_6$ - Evidence for a Pseudo Jahn-Teller Distorted Ground-State. *J. Phys. Chem. Solids* **1990**, *51*, 189−196.

(28) Dan, S.; Maiti, A.; Chatterjee, S.; Pal, A. J. Origin of Bandgap Bowing in Cs$_2$Na$_{1-x}$Ag$_x$BiCl$_6$ Double Perovskite Solid-State Alloys: A Paradigm through Scanning Tunneling Spectroscopy. *J. Phys-Condens Mat* **2021**, *33*, 485701.

(29) Majher, J. D.; Gray, M. B.; Strom, T. A.; Woodward, P. M. $Cs_2NaBiCl_6:Mn^{2+}$ - A New Orange-Red Halide Double Perovskite Phosphor. *Chem. Mater.* **2019**, *31*, 1738−1744.

(30) Shi, H. L.; Du, M. H. Discrete Electronic Bands in Semiconductors and Insulators: Potential High-Light-Yield Scintillators. *Phys. Rev. Appl.* **2015**, *3*, 054005.

(31) Hu, Q. S.; Niu, G. D.; Zheng, Z.; Li, S. R.; Zhang, Y. A.; Song, H. S.; Zhai, T. Y.; Tang, J. Tunable Color Temperatures and Efficient White Emission from $Cs_2Ag_{1-x}Na_xIn_{1-y}Bi_yCl_6$ Double Perovskite Nanocrystals. *Small* **2019**, *15*, 1903496.

(32) Zhou, J.; Rong, X. M.; Zhang, P.; Molokeev, M. S.; Wei, P. J.; Liu, Q. L.; Zhang, X. W.; Xia, Z. G. Manipulation of Bi^{3+}/In^{3+} Transmutation and Mn^{2+}-Doping Effect on the Structure and Optical Properties of Double Perovskite $Cs_2NaBi_{1-x}In_xCl_6$. *Adv. Opt Mater.* **2019**, *7*, 1801435.

(33) Yang, B.; Mao, X.; Hong, F.; Meng, W. W.; Tang, Y. X.; Xia, X. S.; Yang, S. Q.; Deng, W. Q.; Han, K. L. Lead-Free Direct Band Gap Double-Perovskite Nanocrystals with Bright Dual-Color Emission. *J. Am. Chem. Soc.* **2018**, *140*, 17001−17006.

(34) Larnba, R. S.; Basera, P.; Bhattacharya, S.; Sapra, S. Band Gap Engineering in $Cs_2(Na_xAg_{1-x})BiCl_6$ Double Perovskite Nanocrystals. *J. Phys. Chem. Lett.* **2019**, *10*, 5173−5181.

(35) Zhang, G. Y.; Wang, D. Y.; Lou, B. B.; Ma, C. G.; Meijerink, A.; Wang, Y. H. Efficient Broadband Near-Infrared Emission from Lead-Free Halide Double Perovskite Single Crystal. *Angew. Chem. Int. Edit* **2022**, *61*, e202207454.

(36) Pei, Y. F.; Tu, D. T.; Li, C. L.; Han, S. Y.; Xie, Z.; Wen, F.; Wang, L. P.; Chen, X. Y. Boosting Near-Infrared Luminescence of Lanthanide in $Cs_2AgBiCl_6$ Double Perovskites via Breakdown of the Local Site Symmetry. *Angew. Chem. Int. Edit* **2022**, *61*, e202205276.

(37) Li, J. B.; Yan, F. R.; Yang, P. Z.; Duan, Y. Y.; Duan, J. L.; Tang, Q. W. Suppressing Interfacial Shunt Loss via Functional Polymer for Performance Improvement of Lead-Free $Cs_2AgBiBr_6$ Double Perovskite Solar Cells. *SOL RRL* **2022**, *6*, 2100791.

(38) Aydin, E.; Bastiani, M.; Wolf, S. Defect and Contact Passivation for Perovskite Solar Cells. *Adv. Mater.* **2019**, *31*, 1900428.

(39) Locardi, F.; Sartori, E.; Buha, J.; Zito, J.; Prato, M.; Pinchetti, V.; Zaffalon, M. L.; Ferretti, M.; Brovelli, S.; Infante, I.; De Trizio, L.; Manna, L. Emissive Bi-Doped Double Perovskite $Cs_2Ag_{1-x}NaxInCl_6$ Nanocrystals. *ACS Energy Lett.* **2019**, *4*, 1976−1982.

(40) Shi, J. D.; Ge, W. Y.; Tian, Y.; Xu, M. M.; Gao, W. X.; Wu, Y. T. Enhanced Stability of All-Inorganic Perovskite Light-Emitting Diodes by A Facile Liquid Annealing Strategy. *Small* **2021**, *17*, 2006568.

(41) Shi, J. D.; Ge, W. Y.; Gao, W. X.; Xu, M. M.; Zhu, J. F.; Li, Y. X. Enhanced Thermal Stability of Halide Perovskite $CsPbX_3$ Nanocrystals by A Facile TPU Encapsulation. *Adv. Opt Mater.* **2020**, *8*, 1901516.

(42) Wright, A. D.; Verdi, C.; Milot, R. L.; Eperon, G. E.; Perez-Osorio, M. A.; Snaith, H. J.; Giustino, F.; Johnston, M. B.; Herz, L. M. Electron-Phonon Coupling in Hybrid Lead Halide Perovskites. *Nat. Commun.* **2016**, *7*, 11755.

⊞ Recommended by ACS